nature communications



Article

https://doi.org/10.1038/s41467-025-59624-2

Chelated tin halide perovskite for nearinfrared neuromorphic imaging array enabling object recognition and motion perception

Received: 13 December 2024

Accepted: 29 April 2025

Published online: 07 May 2025



Check for updates

Tianhua Liu^{1,4}, Ziguan Yuan^{1,4}, Lixia Wang¹, Cong Shan¹, Qinglin Zhang², Hao Chen¹, Hao Wang¹, Weitong Wu¹, Le Huang², Yang Chai ^{® 3} ⊠ & Xiangyue Meng [®]¹⊠

Neuromorphic imaging arrays integrate sensing, memory, and processing for efficient spatiotemporal fusion, enabling intelligent object and motion recognition in autonomous and surveillance systems. Halide perovskites offer potential for neuromorphic imaging by regulating photogenerated ions and charges, but lead toxicity and limited response range remain key limitations. Here, we present lead-free non-toxic formamidinium tin triiodide perovskites functionalized with bio-friendly quercetin molecules via a multi-site chelate strategy, achieving favorable near-infrared response and optoelectronic properties. Leveraging a non-equilibrium photogenerated carrier strategy, the formamidinium tin triiodide-quercetin based near-infrared optoelectronic synapses exhibit key synaptic features for practical applications, including quasi-linear time-dependent photocurrent generation, prolonged photocurrent decay, high stability, and low energy consumption. Ultimately, a 12 × 12 real-time neuromorphic near-infrared imaging array is constructed on thinfilm transistor backplanes, enabling hardware-level spatiotemporal fusion for robust object recognition and motion perception in complex environments for autonomous and surveillance systems.

Imaging arrays are pivotal components in modern electronic devices, supporting applications ranging from everyday digital photography to advanced autonomous driving^{1,2}. With increasing demand for sensors that can effectively process, store data, and execute computational tasks within the sensor architecture, the need for in-sensor intelligent imaging with low power consumption, high efficiency, and reduced redundant data is growing³⁻⁵. The current state of charge-coupled device (CCD) and complementary metal oxide semiconductor (CMOS) image sensors, which primarily rely on photodetectors, lacks the essential computational, memory and temporal data fusion capabilities, thereby hindering their capability to perform intelligent imaging^{6,7}. In contrast, bio-inspired visual systems based on neuromorphic imaging arrays integrate photonic perception, memory, and process capability, thereby enabling intelligent imaging with efficient spatial and temporal data fusion, surpassing the limitations of conventional CCD and CMOS image sensors⁸⁻¹⁰. Optoelectronic synapses, as the fundamental building blocks for hardware-based neuromorphic imaging arrays, play a critical role in mimicking the complex functionalities of biological synapses^{4,10-13}. Advanced optoelectronic synapses, characterized by favorable optoelectronic properties, such

¹School of Optoelectronics, Center of Materials Science and Optoelectronics Engineering, University of Chinese Academy of Sciences, Beijing, China. ²School of Materials and Energy, Guangdong University of Technology, Guangzhou, China. 3Department of Applied Physics, The Hong Kong Polytechnic University, Hong Kong, China. ⁴These authors contributed equally: Tianhua Liu, Ziguan Yuan. e-mail: y.chai@polyu.edu.hk; mengxiangyue@ucas.ac.cn

as quasi-linear time-dependent photocurrent generation¹⁴, prolonged photocurrent decay, and low energy consumption, are pivotal for energy-efficient neuromorphic imaging, which facilitate the fusion of spatiotemporal information for the purpose of object recognition, enhancement, and motion perception in autonomous vehicles and surveillance systems^{15–17}.

Solution-processed organic materials, quantum dots, halide perovskites, two-dimensional Van der Waals materials, and metal oxides are currently under active investigation as potential candidates for next-generation neuromorphic imaging technologies^{14,18-22}. Among these, halide perovskites hold significant promise due to their capacity to simultaneously manipulate photogenerated ions and electronic charges, thereby facilitating the development of sophisticated neuromorphic imaging systems based on the intrinsic material dynamics^{23,24}. Halide perovskites combine the performance metrics of inorganic semiconductors with the flexibility and adaptability of organic materials²⁵, rendering them an ideal platform for neuromorphic imaging applications, effectively overcoming the limitations inherent in traditional CCD and CMOS sensors. For example, Lee et al. fabricated the artificial synapse using organometal halide perovskite (CH₃NH₃PbBr₃) to mimic key biological synapse principles²⁶. Han et al. demonstrated a floating-gate optoelectronic synaptic transistor using CsPbBr₃ perovskite quantum dots (QDs)²⁷. Sun et al. presented a neuromorphic imaging array using a combination of carbon nanotubes and CsPbBr₃ perovskite QDs²⁸. Guo et al. realized intrinsically stretchable neuromorphic vision-adaptive transistors employing the CsPbBr₃ perovskite QDs and elastomers²⁹. Li et al. obtained a stable two-terminal optoelectronic synaptic based on the ion migration energy barrier and readout signal modulation³⁰. These findings highlight the crucial significance of halide perovskite materials, which are currently at the forefront of neuromorphic imaging research due to their favorable properties.

Despite considerable progress, several critical issues for advanced neuromorphic imaging applications remain unresolved. First, benefiting from the favorable penetration capability of near-infrared (NIR) light through haze, smoke, and plastic, NIR-responsive optoelectronic synapses are crucial for intelligent autonomous driving in challenging environmental conditions, especially low-visibility conditions³¹. However, reported perovskite-based optoelectronic synapses suffer from a limited response range (ultraviolet-visible)32,33. And NIR-responsive real-time neuromorphic imaging arrays have not been implemented, limiting their application in intelligent autonomous driving. Second, most reported perovskite optoelectronic synapses are based on toxic lead-based perovskites, rendering them unsuitable for biocompatible applications^{34,35}. Third, the replacement of lead (Pb) with tin (Sn) in perovskite materials mitigates toxicity concerns and extends the response wavelength into the NIR region³⁶⁻³⁸. Nonetheless, the Sn²⁺ oxidation and the rapid crystallization rate of tin-based perovskites leads to a high density of defects, thereby elevating non-radiative recombination losses^{39,40}. This causes higher energy consumption and reduced synaptic performance. Most importantly, achieving key parameters like quasi-linear time-dependent photocurrent generation remains challenging in neuromorphic imaging for object recognition, enhancement, and motion perception in autonomous vehicles and surveillance systems^{6,14,15}, limited by the device mechanisms such as photo-induced ion migration, phase transition, ferroelectric domain reconfiguration and the trapping of photogenerated carriers⁴¹. It is essential to address these challenges to improve the applicability and safety of perovskite materials in neuromorphic imaging technologies.

In this work, the bio-friendly quercetin (QR) molecules are introduced to multi-site chelate with $\rm Sn^{2^+}$ in the non-toxic $\rm CH(NH_2)_2Snl_3$ (FASnl₃) perovskites films. The robust multi-site chelation effect significantly reduces the crystallization rate of FASnl₃ perovskite films and suppresses $\rm Sn^{2^+}$ oxidation, yielding films with significantly reduced trap density. Coupled with the device mechanism of non-equilibrium

photogenerated carrier strategy, the NIR optoelectronic synapse based on FASnI₃-OR perovskite films exhibits enhanced optoelectronic synaptic characteristics, such as quasi-linear time-dependent photocurrent generation, prolonged photocurrent decay, and low energy consumption. These features are crucial for enabling efficient, lowpower intelligent neuromorphic imaging that overcomes the limitations of traditional image sensors. Furthermore, the 12 × 12 real-time neuromorphic NIR imaging array is successfully constructed on the thin-film transistor (TFT) backplanes, enabling spatiotemporal information fusion for object recognition, enhancement, and motion perception in complex environments for autonomous vehicles and surveillance systems at the hardware level, through the heterogeneous integration of perovskite optoelectronic devices and Si electronic circuits. This work establishes a versatile platform for NIR optoelectronic synapses based on lead-free perovskites, paving the way for advanced neuromorphic imaging technologies in autonomous systems and offering strategic guidance for realizing high-performance NIR optoelectronic synapses.

Results

Chelation between quercetin and tin-based perovskite

In order to gain a comprehensive understanding of the interaction between QR molecules and FASnI₃ perovskite, the electrostatic potential (ESP) of the QR molecule was analyzed by density functional theory (DFT) calculations (Supplementary Fig. 1). The QR molecule demonstrates low ESP (blue) on the hydroxy and carbonyl groups, indicating the strong interaction with the positively charged Sn²⁺. As depicted in Fig. 1a, the QR molecule provides numerous coordination bonds with Sn²⁺, and the most probable chelation sites are formed by two adjacent coordination bonds⁴². Accordingly, the QR molecule was chelated with Sn via Sn-O bonds, forming the stable five-membered ring. Furthermore, owing to the multi-site chelation effects, the QR molecule exhibits a significant binding energy (150.52 kJ mol⁻¹) with the FASnl₃ perovskite lattice, indicating a robust interaction with the Snl₆ framework (Fig. 1b). The chelation effects are further confirmed by liquid-state ¹H nuclear magnetic resonance (NMR) measurements. As depicted in Fig. 1c, the resonance signals attributed to the hydroxy group at positions 1, 2, 3, and 4 in the QR molecule were evidently broad subsequent to the incorporation of SnI₂ into the QR sample in deuterated dimethyl sulfoxide-d₆ (DMSO-d₆) (Supplementary Fig. 2). The broad line widths indicate a restricted motion in the QR molecule, originating from the strong multi-site chelation effects between the Sn²⁺ and hydroxy groups, which keep the position of the H atom fixed in the hydroxy group (Supplementary Figs. 3-5). According to Fourier transform infrared (FTIR) spectroscopy, the stretching vibration peak of the hydroxy group in the QR molecule shifts from 3370 to 3303 cm⁻¹ after the addition of SnI₂ (Fig. 1d). And the stretching vibration peak of the carbonyl group also shifts from 1656 to 1641 cm⁻¹ subsequent to the addition of SnI₂ (Fig. 1d and Supplementary Fig. 6). These findings further validate the strong multi-site chelation effects observed between the Sn2+ and QR molecules. From the ultraviolet-visible (UV-Vis) absorption spectrum, the pristine QR sample in dimethyl sulfoxide (DMSO) exhibits two main absorption peaks at 379 and 261 nm, which were attributed to the $\pi \rightarrow \pi^*$ electron transition of the A ring and the $n \rightarrow \pi^*$ electron transition of the B ring, respectively (Supplementary Fig. 7)⁴³. As shown in Fig. 1e, two main absorption peaks shift to 460 and 276 nm after adding SnI₂, indicating that the QR molecule interacts with both the A and B rings. This further confirms the existence of multi-site chelation interaction between the FASnI₃ and QR molecules. The photoluminescence (PL) observed in the QR solution is frequently associated with the excited state intramolecular proton transfer⁴⁴. As depicted in Fig. 1f, the intensity and shape of the PL peak in the QR solution undergo a significant change subsequent to the addition of SnI₂, which was attributed to the strong multi-site chelation effects between Sn²⁺ and the QR molecule.

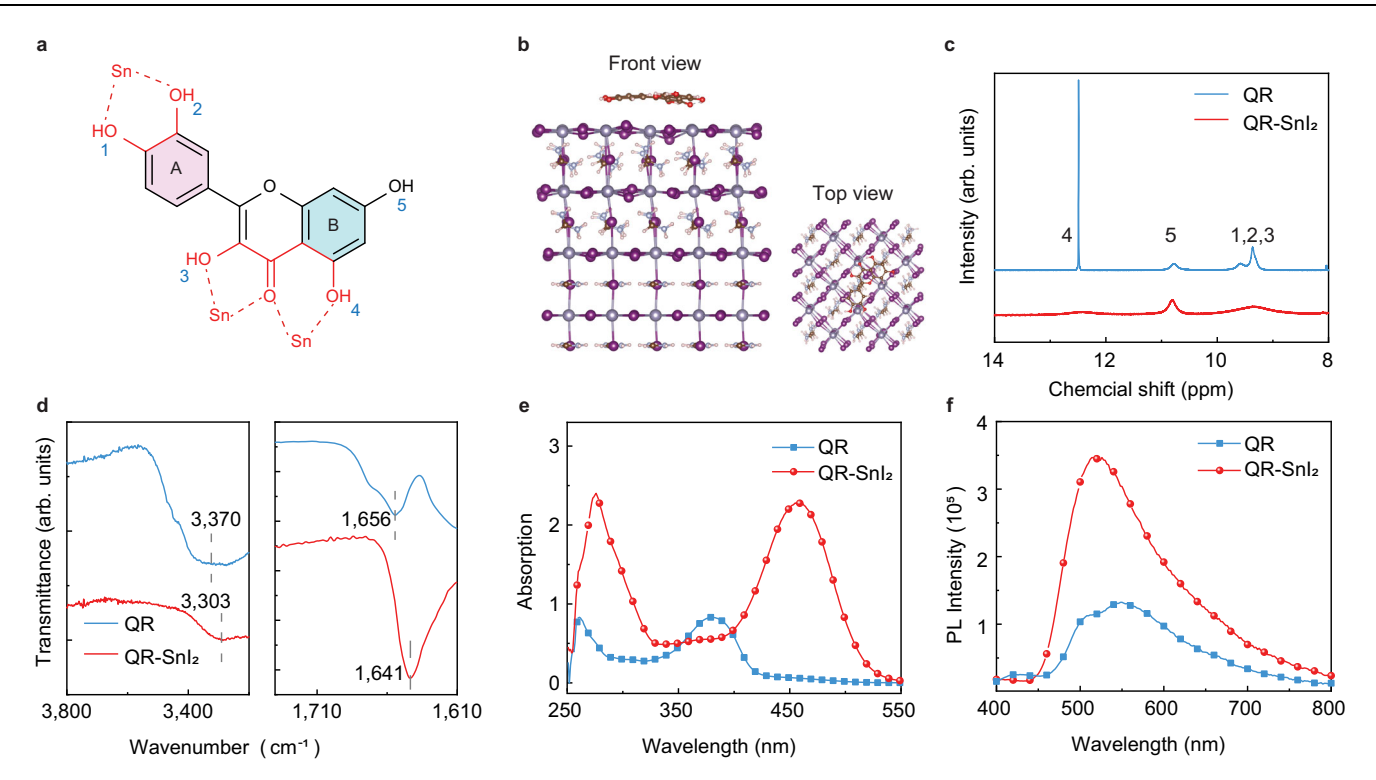


Fig. 1 | Chelation interactions between QR molecule and FASnl $_3$ perovskite. a Molecular structure of QR and chelation sites. b Geometry-optimized structure of QR molecules on perovskite surface using DFT calculations: c 1 H NMR spectra of QR

and QR-Snl₂ in DMSO- d_6 solution. **d** FTIR spectra of QR and QR-Snl₂. **e** UV–Vis absorption spectra of QR and QR-Snl₂ in the DMSO solution. **f** PL spectra of QR and QR-Snl₂ in the DMSO solution.

Characterization of chelated tin based perovskite films

In order to understand the effect of multisite chelation on crystal growth, in situ PL spectroscopy is conducted during the spin coating procedure of the FASnI₃ and FASnI₃-QR perovskite films (Fig. 2a, b). After dropping the anti-solvent at 52 s, PL signals emerge, accompanied by a broadening of the PL spectrum, indicating the formation of FASnI₃ perovskite crystals. According to Fig. 2c, FASnI₃-QR perovskites require a longer duration to attain the saturation intensity of PL than pristine FASnI₃ perovskites, indicating a slower crystal growth rate in FASnI₃-QR perovskites³⁷. This is attributed to the strong multi-site chelation effects between the Sn2+ and QR molecules. Subsequently, for pristine FASnI₃ perovskites, the PL intensity exhibits a sudden drop and ~85% of the intensity is quenched within 10 s, which can be attributed to the rapid aggregation of perovskite crystals during crystal growth. During the rapid aggregation process, the defect-rich amorphous regions can be formed due to the imperfect arrangement of the FASnI₃ perovskite crystals, leading to non-radiative recombination. In contrast, for FASnl₃-QR perovskites, the fast PL drop completely disappears⁴⁵. This indicates that the rapid aggregation process is inhibited, resulting in FASnI₃-QR films with less trap and reduced fluorescence quenching due to the strong multi-site chelation effects between the Sn²⁺ and QR molecule. To summarize, the incorporation of QR molecules slow down the crystal growth rate and inhibits the disordered aggregation process during crystal growth through a strong multi-site chelation interaction with FASnI₃ perovskite, ultimately leading to high-quality FASnI₃-QR films with less trap density.

The primary sources of defects in tin-based perovskite films are identified as Sn vacancies and Sn²⁺ oxidation. Furthermore, the effect of the multisite chelation interaction on Sn vacancy formation and Sn²⁺ oxidation is investigated (Fig. 2d). Using the DFT calculations, the formation energy of Sn vacancies increases from 0.55 to 0.96 eV after the introduction of the QR molecule (Supplementary Fig. 8). According to X-ray photoelectron spectroscopy results, the Sn²⁺ content in the FASnI₃ perovskite films increases from 64% to 81% after the

addition of the QR molecule (Fig. 2d and Supplementary Fig. 9). These results indicate that the addition of QR molecule can inhibit the formation of Sn vacancies and the oxidation of Sn²⁺ through a strong multi-site chelation interaction between Sn²⁺ and OR molecule. thereby reducing the defects in the FASnI₃-QR perovskite films. The exact mechanism behind this stabilization effect by a robust multi-site chelation interaction between Sn²⁺ and QR molecule is investigated. Firstly, after the addition of quercetin, the SnI₂ solution exhibits a noticeable color change (Supplementary Fig. 10), suggesting the formation of a chelation complex. This complex can limit the exposure of Sn²⁺ to oxygen and moisture, thereby preventing the oxidation of Sn²⁺. DFT calculations reveal that the adsorption energy (43.42 kJ mol⁻¹) of oxygen molecules on the FASnI₃ crystal surface is significantly lower than that (150.52 kJ mol⁻¹) of QR molecules on the FASnI₃ crystal surface (Supplementary Fig. 11). This indicates that QR molecules interact more strongly with the FASnI₃ crystal surface, making them more stable on the surface. Consequently, the adsorption of oxygen molecules is effectively inhibited, significantly reducing the risk of Sn²⁺ oxidation. To confirm this, the absorption spectrum of the SnI₂ and Snl₂-QR solutions is measured by exposure to air. Since the oxidation of I to I₃ generally follows the oxidation of Sn²⁺, the emergence rates of the characteristic I₃⁻ absorption peaks at 293 nm and 365 nm serve as indicators for evaluating the extent of Sn²⁺ oxidation⁴⁶. After exposure to air for 60 min, a distinct I₃ peak emerges in the SnI₂ solution, whereas in the SnI₂-QR solution, the I₃ peak appears only after 120 min (Supplementary Fig. 12), indicating enhanced resistance to oxidation. The SnI₂-QR complex is able to reduce Sn²⁺ exposure to oxygen and moisture, effectively preventing the oxidation of Sn²⁺. Furthermore, cyclic voltammetry is used to analyze the redox potentials in a perovskite precursor solution³⁷. In the cyclic voltammetry curves, obvious oxidation and reduction peaks are observed (Supplementary Fig. 13), and the oxidation potential of the SnI₂-QR solution is significantly increased from 1.43 to 1.55 V, suggesting enhanced resistance to Sn²⁺ oxidation and improved stability of the perovskite precursor. These

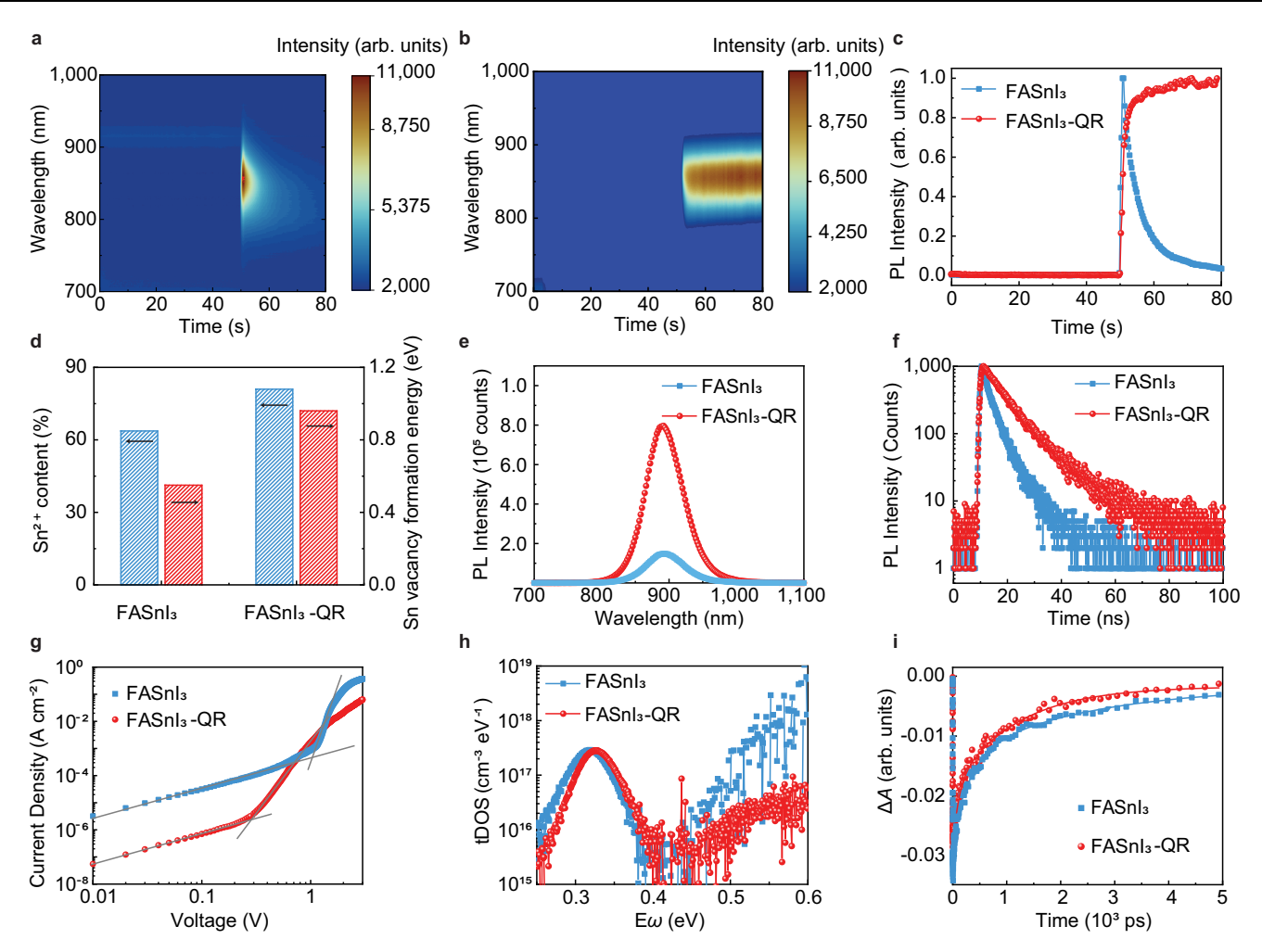


Fig. 2 | Characterizations of the chelated FASnI₃-QR perovskite films. a In situ PL spectra during the spin-coating process for a FASnI₃ and b FASnI₃-QR perovskite films. c PL evolution at 858 nm during spin coating. d The Sn²⁺ content and the formation energy of Sn vacancies in the FASnI₃ and FASnI₃-QR films. e Steady-state

PL spectra of the FASnl₃ and FASnl₃-QR films. **f** TRPL decay spectra of the FASnl₃ and FASnl₃-QR films. **g** Dark current density-voltage curves of the hole-only devices. **h** The tDOS spectra of the FASnl₃ and FASnl₃-QR devices. E_{ω} denotes the trap energy level. **i** The DAS process at 865 nm of the FASnl₃ and FASnl₃-QR films.

results indicate that the QR molecular exhibits multi-site chelation with $\mathrm{Sn^{2^+}}$, potentially forming a stable complex that limits the exposure of $\mathrm{Sn^{2^+}}$ to oxygen and moisture. Furthermore, this complex effectively stabilizes the coordination environment of $\mathrm{Sn^{2^+}}$, reducing the free activity of $\mathrm{Sn^{2^+}}$ ions and increasing the oxidation potential of the tin complex. Consequently, these effects collectively suppress the oxidation of $\mathrm{Sn^{2^+}}$, enhancing the overall stability of FASnl₃ perovskite materials.

Steady-state PL and time-resolved photoluminescence (TRPL) are employed to understand the charge carrier dynamics in the perovskite films. The increased PL intensity and prolonged decay time indicate a reduction in defects and suppression of non-radiative recombination in the FASnI₃-QR perovskite film (Fig. 2e, f), which is consistent with the previous DFT calculations. The PL and TRPL results for varying QR concentrations (from 1 mg mL⁻¹ to 6 mg mL⁻¹) demonstrate that the optimal concentration was 2 mg mL⁻¹ (Supplementary Fig. 14). Additionally, the trap state density is quantified using space-charge-limited current (SCLC) and thermal admittance spectroscopy (TAS) measurements⁴⁷. From SCLC measurements, for hole-only devices, the FASnI₃-QR film presents a lower trap-filled limit voltage (V_{TFI}) of 0.31 V and a reduced hole trap density of 4.75×10^{16} cm⁻³ than those (1.07 V, 1.6×10^{17} cm⁻³) of the pristine FASnI₃ film (Fig. 2g). Similar to electrononly devices, the FASnI₃-QR film also exhibits a lower trap-filled limit voltage (V_{TFL}) and a reduced electron trap density (Supplementary

Fig. 15). The trap density (tDOS) at different energy depths is determined by the TAS methods, which can be calculated as follows.

$$tDOS(E_{\omega}) = -\frac{V_{bi}}{qW} \frac{\omega}{K_{B}T} \frac{dC}{d\omega}$$
 (1)

where ω is the angular frequency, $V_{\rm bi}$ is the built-in potential, T is the absolute temperature, C is the capacitance, W is the depletion width, $K_{\rm B}$ is the Boltzmann constant, and q is the elementary charge, respectively. The trap energy (E_{ω}) was calculated by the Eq. (2).

$$E_{\omega} = K_{\rm B} T \ln \left(\frac{\omega_0}{\omega} \right) \tag{2}$$

where ω_0 is the attempt-to-escape frequency. The FASnl₃-QR devices exhibit lower tDOS values compared to pristine FASnl₃ devices, both in the shallow E_ω range (0.25–0.32 eV) and at deeper E_ω levels (0.40–0.60 eV) (Fig. 2h). TAS spectroscopy is also employed to further characterize defects and charge carrier dynamics in perovskite films⁴⁸. Herein, a 450 nm pump pulse is employed to excite electrons from the ground state to excited states in FASnl₃ perovskite films. The probe light, ranging from 510 to 1000 nm, is used to monitor absorption as a function of wavelength and time. A ground-state bleaching peak is observed at 865 nm, consistent with the steady-state edge-band

absorption, indicating that the transient absorption peak is associated with the lower bandgap of FASnI₃ with or without OR molecule (Supplementary Fig. 16)48. The longer exciton lifetime at the lower bandgap reduces interference from exciton cooling processes. The 865 nm peaks were used to evaluate the quality of FASnI₃ perovskite films using kinetic decay-associated spectra (DAS), fitted with a biexponential function. The fitting parameters include two components, namely τ_1 and τ_2 . The fast component, τ_1 , corresponds to photogenerated carrier trapping at perovskite grain boundaries and internal defects, while the slow component, τ_2 , represents electron-hole recombination. Compared to pristine FASnI₃ films with τ_1 of 330 ps and τ_2 of 2346 ps, the FASnI₃-QR films exhibit faster decay times (τ_1 of 103 ps and τ_2 of 1166 ps), indicating a reduction in grain boundary trapping, defects, and recombination due to a robust multi-site chelation interaction between Sn²⁺ and QR molecule (Fig. 2i). The crystallinity of the perovskite films is investigated through X-ray diffraction (XRD). According to the XRD results, the addition of QR molecules did not significantly change the crystallinity of FASnI₃ films (Supplementary Fig. 17), which is consistent with the grazing incidence wide angle X-ray scattering results (Supplementary Fig. 18). The film morphology is investigated using scanning electron microscope (SEM). The pristine FASnI₃ film is composed of densely packed grains with varying sizes, with noticeable gaps and irregularities between them. The surface morphology is characterized by pronounced undulations and incomplete coverage, indicating numerous defects in the pristine FASnI₃ films⁴⁹. After the addition of QR molecules, the grain structure becomes more uniform, with a significant reduction in the gaps between grains, resulting in a notably smoother and more homogeneous FASnl₃-QR film surface, which contributes to the reduced defects in the FASnI₃-QR film. With further increased concentrations of the QR molecule, a significant reduction in grain size is observed (Supplementary Fig. 19). Thus, the optimal concentration of the QR molecule is determined to be 2 mg mL⁻¹, consistent with the PL and TRPL measurements (Supplementary Fig. 14). The chelated FASnI₂-OR perovskite films, exhibiting a low trap state density and reduced non-radiative recombination, prove to be advantageous for photon-triggered neuromorphic applications as follows.

Near infrared induced neuromorphic behavior

Synapses are the basic connecting units of the human nervous system, typically comprising a presynaptic terminal (formed by the axon of a pre-neuron), a synaptic cleft, and a postsynaptic terminal located at the dendrite of a post-neuron⁵⁰. A optoelectronic synapse comprising the device structure of Si/SiO₂/PEDOT:PSS/FASnI₃ perovskite without or with QR molecule/Au is constructed (Fig. 3a), which enables NIR photon-triggered neuromorphic behavior owing to the extensive absorption range of FASnI₃ perovskite from 400 to 900 nm (Supplementary Fig. 20). Notably, our results demonstrate the NIR-responsive behavior of perovskite-based optoelectronic synapses^{31,32}. The source and drain electrodes operate analogously to the presynaptic and postsynaptic membranes, respectively, while the channel represents the synaptic cleft. Photogenerated carriers serve as neurotransmitters, while photostimulation functions as the action potential. After light stimulation, photogenerated carriers are released, triggering the excitatory postsynaptic current (EPSC).

As shown in Fig. 3b, the staggered heterojunction is formed between the FASnI₃ perovskite and the PEDOT:PSS layer. The energy levels of perovskite and PEDOT:PSS films are measured using ultraviolet photoelectron spectroscopy (Supplementary Fig. 21). The valence band (VB) of FASnI₃-QR perovskite films is –5.12 eV, and the VB value of FASnI₃-QR perovskite films is –5.19 eV. The highest occupied molecular orbital (HOMO) energy level of PEDOT:PSS is determined to be –5.24 eV. Due to the low exciton binding energy of FASnI₃ perovskite, excitons can be readily dissociated into electrons and holes either at the perovskite/PEDOT:PSS interface or within the perovskite

film under light illumination^{51,52}. The dissociated holes prefer to diffuse into the PEDOT:PSS laver, driven by the energy gradient, whereas the electrons are confined within the perovskite layer due to the significant difference in energy level (0.79 eV) between the conduction band (CB) of the FASnI₃ perovskite and the lowest unoccupied molecular orbital level of PEDOT:PSS⁵². Since the electron mobility $(1.7 \times 10^{-4} \text{ cm}^2 \text{ V}^{-1} \text{ s}^{-1})$ of the FASnI₃ perovskite is significantly lower than the hole mobility (5.6 cm² V⁻¹ s⁻¹) of PEDOT:PSS, the channel current under light illumination is predominantly attributed to hole transport facilitated by PEDOT:PSS (Supplementary Fig. 22). Due to the extended lateral and vertical transport distances of the holes, the photocurrent exhibits a slow rise, analogous to the response of a biological synapse. After turning off the light, accumulated photogenerated electrons in perovskite films exhibit a prolonged release time, demonstrating typical EPSC characteristics. Furthermore, defects in FASnI₃ perovskite films may lead to sub-linear time-dependent photocurrent generation and reduced time decay due to increased recombination³⁹. Ultimately, the substantial mobility of hole and electron carriers, resulting from the deliberate incorporation of a high-mobility hole transport layer, is referred to as the non-equilibrium carrier strategy, which subsequently leads to synaptic behavior⁵³. The non-equilibrium carrier strategy, in conjunction with less-defect photoresponsive perovskite films, has the potential to result in quasi-linear time-dependent photocurrent generation and prolonged photocurrent decay, as discussed later. To validate the synaptic behavior resulting from electron accumulation induced by the non-equilibrium carrier strategy, we conduct in situ Kelvin probe force microscopy (KPFM) measurements before and after light exposure (Fig. 3c)²⁷. The pristine FASnI₃ perovskite film exhibits a surface potential of 239 mV, which is decreased to 181 mV under illumination. Generally, a decrease in surface potential results from the accumulation of electrons or the loss of holes²⁷. As previously mentioned, light exposure to the FASnI₃ perovskite film induces photocarrier generation. The photogenerated holes are capable of easily escaping from the perovskite film to PEDOT:PSS due to the energy gradient and favorable hole mobility. Consequently, the photoinduced electrons remain within the FASnI₃ perovskite film, resulting in a significant reduction in surface potential after light exposure.

The FASnI₃ and FASnI₃-QR devices demonstrate fundamental characteristics of synaptic plasticity observed in biological neural networks (Fig. 3d). Under 785 nm NIR light stimulation, the EPSC increases slowly, and decays gradually when the light is turned off. This behavior reflects the manners in which synapses in living organisms respond to stimuli, highlighting the potential of these devices in mimicking neural processes. Nevertheless, the response of these two devices to light reveals a significant disparity. The FASnI₃-QR optoelectronic synapse demonstrates a quasi-linear time-dependent photocurrent generation, whereas the FASnI₃ optoelectronic synapse shows a sub-linear time-dependent photocurrent generation behavior¹⁵. For a quantitative comparison, the quasi-linear time-dependent photocurrent generation can be analyzed using the Eq. (3).

$$I_{ph} = I_1 \left(1 - \exp\left(-\frac{t}{t_1}\right) \right) + I_2 \left(1 - \exp\left(-\frac{t}{t_2}\right) \right)$$
 (3)

where I_1 and I_2 are photocurrent coefficients, and t_1 and t_2 are time constants. The FASnI₃-QR optoelectronic synapse demonstrates a high photocurrent coefficient ratio (I_2/I_1) value of 277, coupled with a prolonged time constant (t_2 = 1.19 s) (Supplementary Table 1). Consequently, the photocurrent generation exhibits a nearly linear progression subsequent to the expansion of the exponential function in a series, approximated as $I_{\text{ph}(t)} \cong I_2(t/t_2)$ (Supplementary Note 1). In contrast, the FASnI₃ optoelectronic synapse shows a significantly lower photocurrent coefficient ratio of 4.1 and a shorter time constant of 0.52 s, which leads to a sub-linear photocurrent response (Fig. 3e and Supplementary Fig. 23)¹⁵. The substantial difference in photoresponse

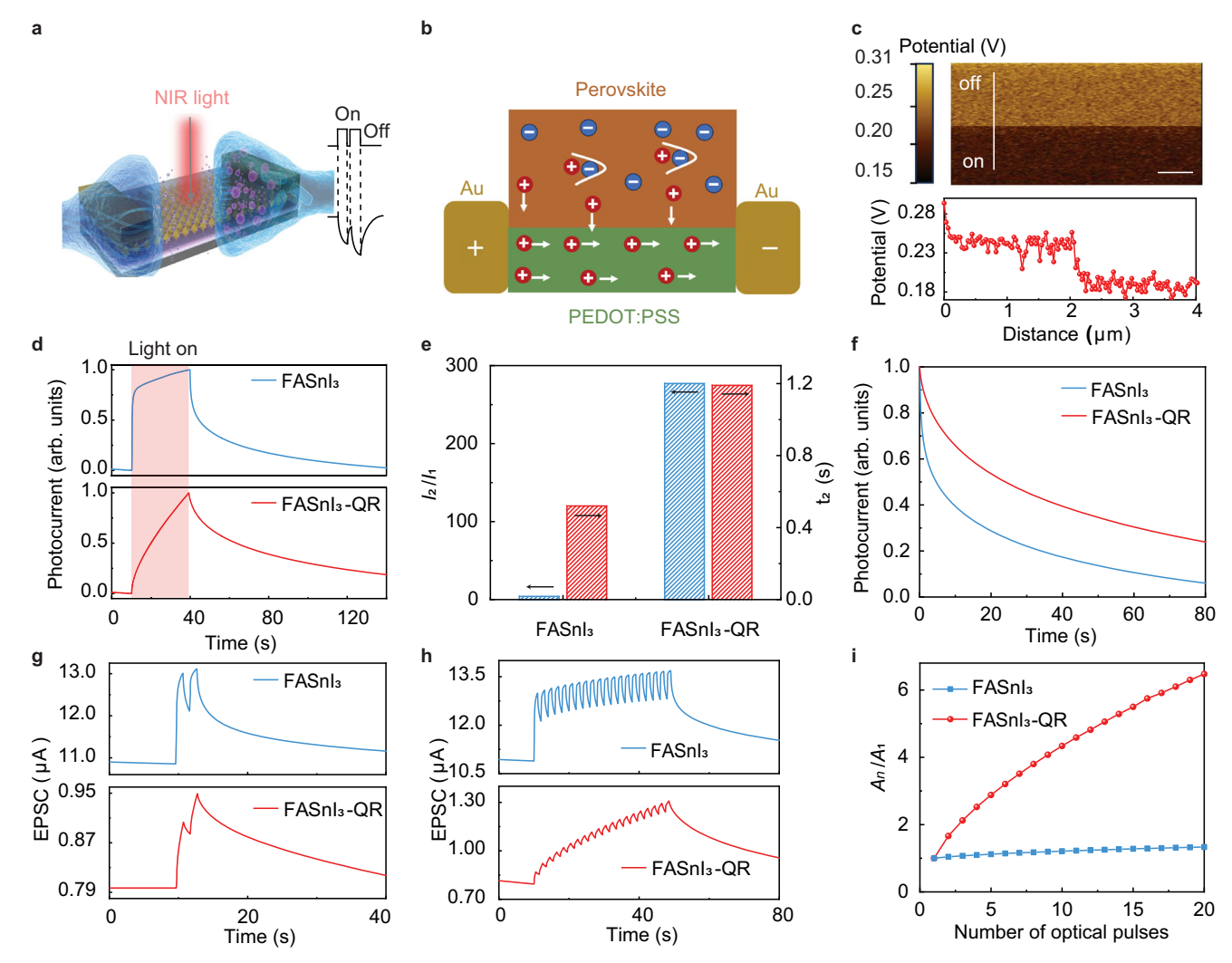


Fig. 3 | **Photon-triggered neuromorphic behavior of the FASnl₃-QR devices. a** Schematic illustration of the device structure. **b** Schematic diagram of synaptic behavior mechanism. **c** Surface potential of the perovskite film before and after light illumination (scale bar, 5 μ m). **d** Photocurrent generation and decay characteristics of the FASnl₃ and FASnl₃-QR devices under 785 nm optical pulses. (70 mW cm⁻², pulse width: 30 s). EPSC refers to the excitatory postsynaptic current. **e** The fitting photocurrent coefficient ratio (I_2/I_1) value and time constant (I_2)

for the FASnl₃ and FASnl₃-QR devices. **f** Normalized photocurrent decay characteristics of the FASnl₃ and FASnl₃-QR devices. **g** PPF behavior of the FASnl₃ and FASnl₃-QR devices under 2 pulses of 785 nm light (70 mW cm⁻², 0.5 Hz, 50% duty). **h** LTP behavior of the FASnl₃ and FASnl₃-QR devices under 20 pulses of 785 nm light (70 mW cm⁻², 0.5 Hz, 50% duty). **i** Evolution of $A_{\rm n}/A_{\rm 1}$ for the FASnl₃ and FASnl₃-QR devices. Unless otherwise specified, a read voltage of 50 mV was applied.

can be attributed to a lower recombination rate, primarily due to the decreased trap density in the FASnI₃-QR devices. In addition, the FASnI₃-QR optoelectronic synapse also demonstrates a prolonged photocurrent decay owing to the reduced recombination in the FASnI₃-QR devices with low trap density (Fig. 3f). Paired-pulse facilitation (PPF) is an important form of short-term synaptic plasticity (STP), characterized by an enhanced postsynaptic response to the second of two closely spaced stimuli¹⁴. Evidently, under 785 nm NIR light stimulation, the PPF value (1.41) of the FASnI₃-QR optoelectronic synapse is higher than that (1.05) of the FASnI₃ optoelectronic synapse, indicating favorable STP due to quasi-linear time-dependent photocurrent generation and prolonged photocurrent decay in the FASnI₃-QR optoelectronic synapse (Fig. 3g). The transition from STP to longterm plasticity (LTP) is dependent on the frequency and intensity of synaptic activity. Hence, LTP is induced subsequent to 20 consecutive stimuli, as depicted in Fig. 3h. It is worth noting that the FASnI₃ device exhibited a larger post-synaptic current value. Due to the smaller band alignment (0.05 eV) between PEDOT:PSS and FASnI₃ perovskite films, photogenerated holes of FASnI₃ devices can more easily diffuse into PEDOT:PSS, resulting in a higher post-synaptic current of the FASnI₃

device. To quantify the contrast between LTP and STP, the synaptic weight (A_n/A_1) is defined as the ratio of the photocurrent generated by n optical pulses (A_n) to that generated by a single pulse $(A_1)^{15}$. The synaptic weight of the FASnI₃-QR optoelectronic synapse increases continuously with the number of optical pulses, whereas that of the control FASnI₃ device experiences a slow increase until it finally reaches saturation (Fig. 3i). The FASnI₃-QR optoelectronic synapse demonstrates a significantly higher synaptic weight $(A_{20}/A_1 = 6.48)$ compared to the FASnI₃ optoelectronic synapse $(A_{20}/A_1 = 1.33)$ subsequent to 20 NIR optical pulses, which is attributed to the quasilinear time-dependent photocurrent generation and prolonged photocurrent decay. The FASnI₃-QR optoelectronic synapse demonstrates favorable STP and LTP, which are advantageous for image preprocessing and neuromorphic imaging¹⁴. Furthermore, compared to the FASnI₃ optoelectronic synapse, the FASnI₃-QR optoelectronic synapse also exhibited low dark current and noise current (Supplementary Fig. 24), as well as favorable environmental stability due to the reduced trap density in the chelated FASnI₃-QR perovskite (Supplementary Fig. 25). To further assess long-term stability, we extend the air exposure duration in our experiments to evaluate

unencapsulated and encapsulated FASnI₃-QR devices under ambient conditions. The unencapsulated device also exhibited good air stability. After 50 min of air exposure, the device retains 80% of its initial ΔEPSC value, while after 60 min of exposure, it retains 50% of its original value (Supplementary Fig. 26). Furthermore, due to the oxidation of Sn²⁺, the ΔEPSC value progressively decreases with prolonged air exposure. The UV-encapsulated FASnl₃-QR devices are sealed with a cover glass using a low-cost epoxy resin (Supplementary Fig. 27). After 24 h of exposure to air, the Δ EPSC values for the encapsulated device show no significant degradation (Supplementary Fig. 28), indicating that the UV-encapsulated device exhibited favorable stability. These findings further suggested the favorable reliability of the device. Photostability is a critical consideration for the practical application of perovskite optoelectronic synapses. Thus, we investigate the absorption spectra of the UV-encapsulated FASnI₃-QR perovskite films under continuous optical illumination (50 mW cm⁻²) in the air. The results demonstrate that the absorption spectra of UVencapsulated FASnI₃-QR perovskite films exhibit no significant changes, indicating favorable photostability (Supplementary Fig. 29). We further examine the photocurrent generation and decay characteristics of unencapsulated FASnl₃-QR devices under continuous 785 nm optical illumination (78 mW cm⁻²) in a vacuum environment (Supplementary Fig. 30). The photostability results demonstrate that after isolating the FASnI₃-QR device from moisture and oxygen, the FASnI₃-QR device exhibits remarkable photostability. Under continuous 785 nm NIR illumination at 78 mW cm⁻² for 24 h, the Δ EPSC values remain stable with no noticeable signs of device failure. Furthermore, the encapsulated FASnI₃-QR device also demonstrated favorable photostability in the air (Supplementary Fig. 31).

According to Hebb's postulate, synaptic weight can be modulated by factors such as the timing, number, duration, frequency, and intensity of optical stimulation, as well as the applied voltage. Consequently, various synaptic properties of the FASnI₃-QR optoelectronic synapse are characterized, including spike-timing-dependent plasticity, spike-number-dependent plasticity (SNDP), spike-duration-dependent plasticity, spike-frequency-dependent plasticity, and spike-voltage-dependent plasticity (Supplementary Fig. 32)⁵⁴. The current level is considered to be the memory state. Notably, STP can be transformed into LTP by reducing the interval between optical pulses, increasing the number and duration of optical pulses, and altering their frequency. For the optoelectronic synapse, energy consumption is an important indicator, which can be obtained from Eq. (4)⁵⁵.

$$E = E_{\text{ele}} + E_{\text{ont}} = V \times I \times t + P \times A \times t \tag{4}$$

where E_{ele} represents the electrical energy consumption, E_{opt} represents the optical energy consumption, V represents the applied bias voltage, I represents the current, P represents the light intensity, A represents the device area, and t is the duration of the optical pulse, respectively. With an applied voltage of 0.02 mV and an optical pulse duration of 520 ms, the electrical energy consumption per synaptic event of the FASnI₃-QR optoelectronic synapse is reduced to 3.84 fJ (Supplementary Fig. 33). This value is among the lowest reported for artificial synapses (Supplementary Table 2), and it is within the energy range of biological synapses (1-10 f) per synaptic event)^{56,57}. The minimum optical energy consumption of the FASnl₃-QR device is measured. With an applied voltage of 0.05 V, an optical pulse duration of 60 ms, device area of $0.002 \, \text{cm}^{-2}$, and light intensity of $1.1 \, \mu\text{W cm}^{-2}$, the optical energy consumption per synaptic event of the FASnI₃-QR optoelectronic synapse is reduced to 0.13 nJ (Supplementary Fig. 34). And the electrical energy consumption per synaptic event is determined to be 0.24 nJ. Notably, the reported energy consumption values are measured with a device area of 0.002 cm². With further reduction in device dimensions, the energy consumption can be further minimized. Furthermore, the FASnI₃-QR optoelectronic synapse exhibits a longer relaxation time of over 1200 s owing to its reduced recombination (Supplementary Fig. 35). The Ebbinghaus forgetting rule has been successfully implemented in the FASnl₃-QR optoelectronic synapse (Supplementary Fig. 36), demonstrating the ability to emulate human memory decay processes at the hardware level.

Neuromorphic imaging and image preprocessing

In neuromorphic image preprocessing, optical response linearity plays a crucial role in enhancing image features by preserving fine details and improving contrast, ultimately contributing to higher recognition accuracy and more robust pattern identification^{58,59}. The FASnI₃-QR optoelectronic synapse demonstrates favorable sublinearity (0.93) compared to the FASnI₃ optoelectronic synapse (1.63), due to the quasi-linear time-dependent photocurrent generation and prolonged photocurrent decay, facilitated by the low trap density in the FASnI₃-QR optoelectronic synapse (Supplementary Fig. 37)¹⁴. Furthermore, a convolutional neural network (CNN) is constructed to simulate handwritten digit recognition using the Modified National Institute of Standards and Technology (MNIST) dataset. The FASnI₃-QR optoelectronic synapse serves as a preprocessing unit that converts gravscale pixel values into current values under optical pulses before the image is input into the network⁶⁰. CNN functions as the image recognition component to identify the processed images. In the experiment, the preprocessed MNIST dataset by the FASnI₃-QR and FASnI₃ devices are used as inputs (Supplementary Fig. 38)61. During the image preprocessing process, the optoelectronic synapse with high optical response linearity allows the preprocessed image to retain more details in low-pixel-value regions and enhance contrast. As a result, preprocessing with a high optical response linearity device can achieve higher recognition accuracy. Thus, after 400 training epochs (Supplementary Fig. 39), the recognition accuracy of the FASnI₃-QR optoelectronic synapse (90.53%) was notably higher than that of the FASnl₃ optoelectronic synapse (79.86%), owing to the lower sublinearity of the FASnI₃-QR optoelectronic synapse. Based on the confusion matrix results obtained during the training process, both devices successfully recognize digits from 0 to 9. Nevertheless, owing to the lower sublinearity value, FASnI₃-QR optoelectronic synapses demonstrate higher recognition accuracy across all digit classes compared to the FASnI₃ optoelectronic synapse (Supplementary Fig. 40). These results demonstrate the potential of FASnI₃-QR optoelectronic synapses for advanced neuromorphic image preprocessing, with enhanced synaptic performance and recognition accuracy.

The optoelectronic synaptic device enables non-contact, lowpower, and stable Morse code encoding by integrating sensing, storage, and processing, ensuring high accuracy and long-term reliability⁶². The optoelectronic synaptic device demonstrates a high capability to distinguish different alphabets encoded in Morse code through variations in EPSC responses. Specifically, each letter is encoded using a sequence of short (point) and long (line) optical pulses, which trigger distinct EPSC peaks in terms of count and amplitude⁶³. To further demonstrate the application of the FASnI₃-QR optoelectronic synaptic device in Morse code encoding, we successfully encode all 26 English letters using distinct sequences of short (point) and long (line) optical pulses. Specifically, a 10-s 785 nm optical pulse generates a low EPSC amplitude, representing a point, while a 40-s 785 nm pulse produces a high EPSC amplitude, corresponding to a line (Supplementary Fig. 41a). Letters are encoded through combinations of point and line. The EPSC-time curves exhibit clear differences corresponding to different letters (Supplementary Fig. 41b). The number of EPSC peaks reflects the number of pulses applied, while the peak amplitude is influenced by pulse duration and device memory effects. Furthermore, by utilizing synaptic plasticity properties such as STP and LTP, the device can accumulate and differentiate signals over time, improving recognition accuracy. The integration of SNDP also

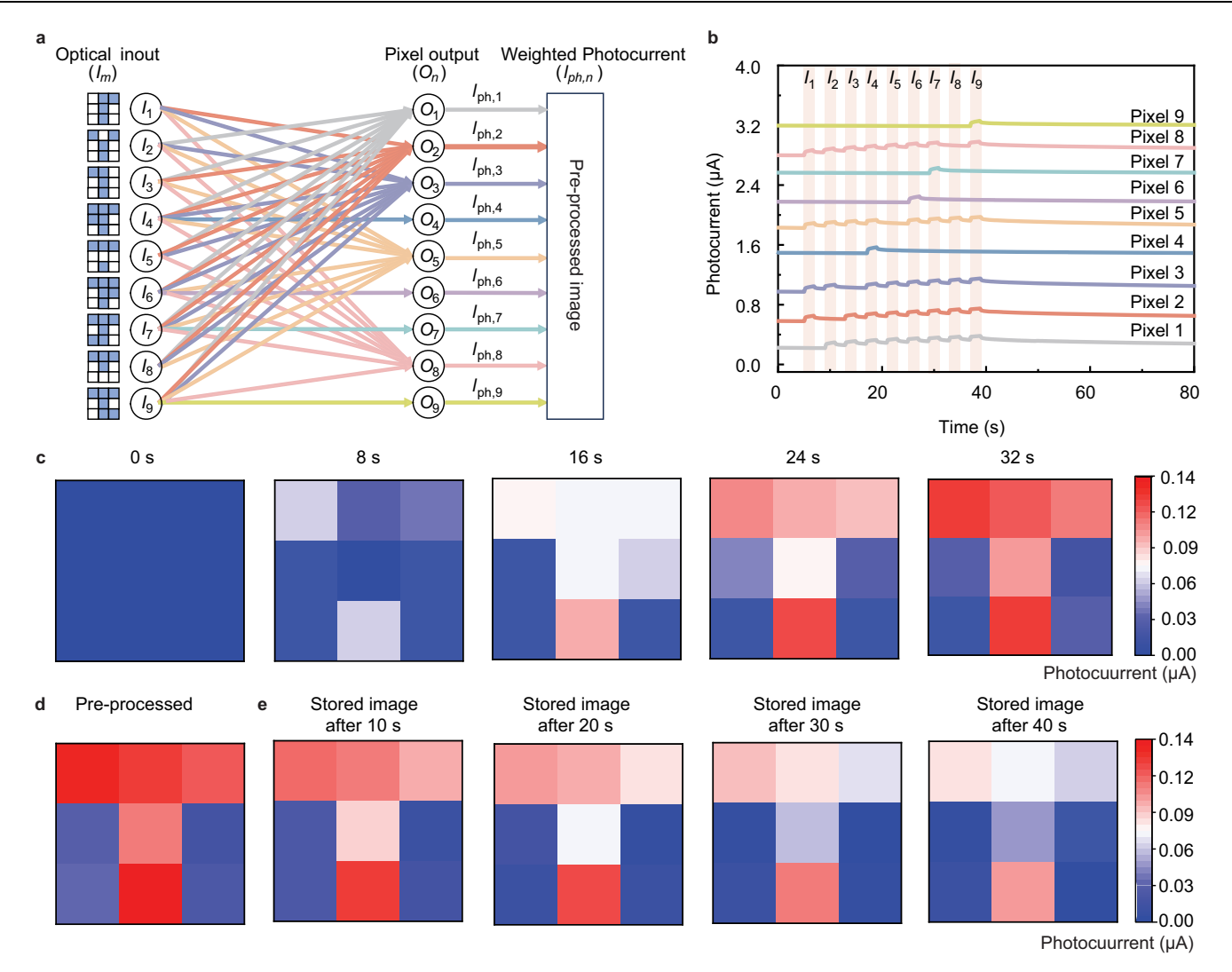


Fig. 4 | **Neuromorphic imaging and image preprocessing enabled by FASnl**₃-**QR optoelectronic synapses. a** Schematic diagram of image preprocessing using a 3×3 FASnl₃-**QR** optoelectronic synapses array. **b** Photocurrent at each pixel of the array under 785 nm NIR light illumination. I_m represents a single 785 nm NIR noisy optical input pulse with a duration of 2 s. O_n denotes the n-th pixel in the array. And

 $l_{ph,n}$ is the corresponding weighted photocurrent generated under optical stimulation. **c** Captured image at various time intervals. **d** Preprocessed image obtained from acquisition and data processing. **e** Stored preprocessed image with gradually decaying photocurrents in individual pixels.

enhances character decoding precision. This demonstration highlights the practical potential of FASnI₃-QR optoelectronic synapses for NIR optical communication and neuromorphic information processing applications.

To demonstrate the neuromorphic imaging and image preprocessing capabilities of the FASnI₃-QR optoelectronic synapses at the hardware level, a 3×3 array is constructed, which enables the extraction of essential image information from extensive noisy optical inputs (Fig. 4a). The original image represents the character "T", with any extra or missing pixels being interpreted as noise (Supplementary Fig. 42). When subjected to a sequence of nine 785 nm NIR noisy optical inputs $(I_m, 2s \text{ per pulse})$, each pixel (O_n) generates a corresponding weighted photocurrent $(I_{ph,n})$. Due to the quasi-linear timedependent photocurrent generation and prolonged photocurrent decay of the FASnI₃-QR optoelectronic synapses, the pixels forming the character "T" $(O_1, O_2, O_3, O_5, O_8)$ receive eight out of the nine 785 nm NIR optical pulses, resulting in a substantial accumulated photocurrent (Fig. 4b). In contrast, the noisy pixels (O_4, O_6, O_7, O_9) are exposed to only one 785 nm NIR optical pulse, producing a negligible photocurrent. By mapping these final photocurrent values, the preprocessed image is successfully reconstructed¹⁵. The mapped images

at various time intervals demonstrate progressively enhanced contrast and reduced noise as the optical input increases (Fig. 4c). Ultimately, a preprocessed image of the letter "T" is derived from noisy optical inputs. This image is retained and slowly fades (Fig. 4d), mimicking synaptic behaviors of memory and forgetting in neural networks.

Neuromorphic object recognition and motion perception

In contrast to visible (Vis) and ultraviolet (UV) light, NIR light exhibits significantly greater penetration capabilities through materials such as glass, plastic, smoke, and haze. This has rendered NIR photodetectors imperative for the advancement of autonomous driving, particularly in challenging conditions such as nighttime, fog, and low visibility, where conventional visible-light sensors are inadequate. By harnessing the favorable penetration of NIR light, NIR photodetectors are capable of reliably identifying crucial objects in complex environments, resulting in a more precise and clearer understanding of the driving scene. Nevertheless, traditional NIR photodetectors lack in-sensor computational and spatiotemporal information fusion capabilities due to the absence of photon-triggered neuromorphic behavior (Supplementary Fig. 43). In contrast, the FASnI₃-QR optoelectronic synapse exhibits favorable NIR photon-triggered neuromorphic behavior, enabled by

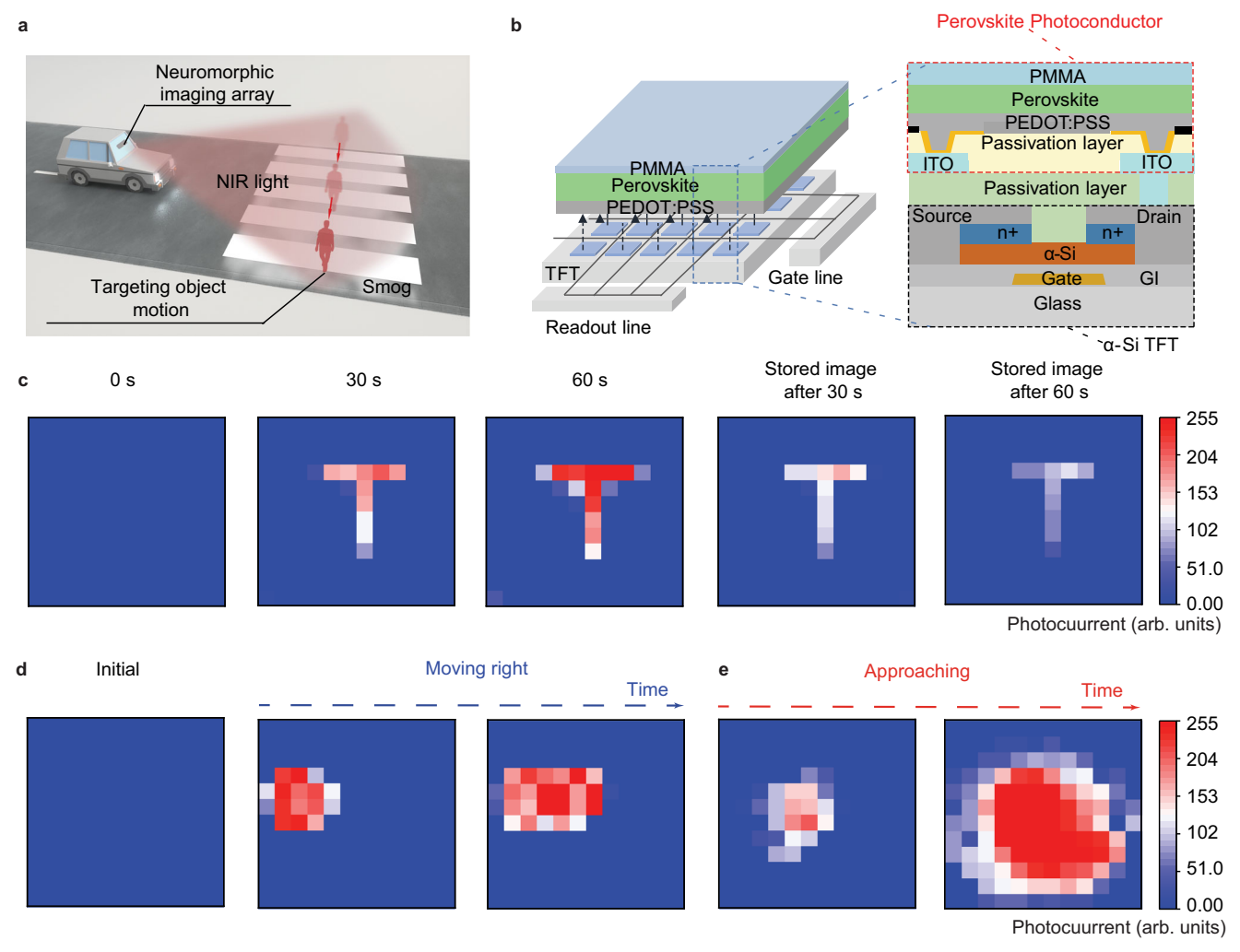


Fig. 5 | Object recognition and in-sensor motion perception in complex environments. a Schematic diagram of neuromorphic NIR imaging array applications for autonomous driving scenarios. b Schematic structure of neuromorphic NIR imaging array based on chelated FASnI₃-QR perovskite. c Captured

NIR image at various time intervals under 785 nm light (target object obscured by A4 paper). **d** The photocurrent mapping for left-to-right motion under 785 nm light. **e** The photocurrent mapping for approaching motion under 785 nm light.

quasi-linear time-dependent photocurrent generation and prolonged photocurrent decay features, thus providing in-sensor computational and spatiotemporal information fusion for object recognition, object enhancement, and in-sensor motion perception in complex environments (Fig. 5a). Such advances could revolutionize perception in autonomous driving, making it as intelligent and adaptive as the human brain^{64,65}.

As depicted in Fig. 5b, the neuromorphic imaging array based on chelated FASnl₃-QR perovskite, consisting of 12×12 (144) pixels, is constructed on a TFT backplane. The drain electrode of the TFT backplane is connected to an indium tin oxide (ITO) layer, serving as the bottom electrode (Supplementary Fig. 44). The TFT array is integrated with an image readout circuit chip to facilitate efficient image acquisition, enabling the heterogeneous integration of perovskite optoelectronic devices and Si electronic circuits for enhanced performance and functionality⁶⁶. To ensure stability, the fabricated arrays are encapsulated to provide insulation against water and oxygen. The neuromorphic imaging array exhibits low photo response non-uniformity value (31%) and dark response non-uniformity value (34%), indicating good uniformity (Supplementary Fig. 45). To demonstrate target recognition and enhancement in complex conditions of autonomous driving, such as haze, smoke, and low visibility, an A4 paper is placed between the NIR light source (785 nm) and the array to simulate the presence of a target object within an obscured environment. The target object is a metal mask with a hollow "T" shape. The 785 nm NIR light can easily pass through A4 paper made of cellulose due to its strong penetration capability, whereas visible light is readily blocked (Supplementary Fig. 46). The mapped 785 nm NIR images at different time intervals behind the A4 paper demonstrate clear patterned shapes and progressively enhanced contrast with increasing illumination time (Fig. 5c), which can be attributed to NIR photon-triggered neuromorphic behavior featuring quasi-linear time-dependent photocurrent generation and prolonged decay. This could contribute to real-time object recognition and enhancement in complex environments for autonomous driving, such as nighttime, fog, and low visibility⁶⁷. The mapped NIR images are retained and gradually faded, emulating synaptic memory and forgetting behaviors at the hardware level, which can enable learn and remember previous scenes and make intelligent decisions based on previous information for autonomous driving. In contrast, the mapped 450 nm VIS images provide no information due to the strong VIS light absorption of the A4 paper (Supplementary Fig. 47). This indicates that the neuromorphic imaging array responsive to VIS light is unable to achieve object recognition and enhancement in complex environments. The mapped 785 nm NIR images without A4 paper also show enhanced contrast and a gradual forgetting characteristic similar to that of biological organisms (Supplementary Fig. 48).

Motion perception holds paramount importance in autonomous driving as it accurately predicts the motion paths of the surrounding dynamic objects, thereby enabling timely responses that enhance safety and adaptability in intricate traffic scenarios 57,67,68. The real-time in-sensor motion perception is successfully realized in the neuromorphic NIR imaging array based on chelated FASnI₃-QR perovskite (Fig. 5d, e). We present a neuromorphic imaging array utilizing perovskite materials for real-time motion perception at the hardware level (Supplementary Table 3). Notably, 785 nm NIR light is used to further enhance motion perception in complex environments, such as nighttime, fog, and low visibility. The moving target is a circular aperture with a diameter of 4.8 mm. With the quasi-linear time-dependent photocurrent generation and prolonged decay characteristics, the photocurrent gradually decays over time following optical stimulation during object movement. The photocurrent observed post-movement is higher than that observed prior to the movement. The neuromorphic NIR imaging array efficiently consolidates spatiotemporal motion information by encoding it through distinct photocurrent levels, thereby enabling clear visualization of the contour for the entire motion trajectory from left to right (Fig. 5d and Supplementary 49)⁶. In comparison, conventional image sensors are limited in their ability to capture a static end-result of motion and lack the capability to integrate temporal information⁶. The neuromorphic NIR imaging array can also perceive approaching and leaving motion. As the object approached the light source, its projected size within the field of view enlarged, accompanied by an expanding photocurrent profile (Fig. 5e and Supplementary 50). Conversely, as the object receded, the photocurrent profile contracted accordingly (Supplementary Fig. 51). Based on the magnitude of the photocurrent profile, the approaching and leaving motions were deduced6.

Discussion

In summary, we achieve less-trap FASnI₃ perovskite films with effective NIR response and non-toxicity through multi-site chelation effects employing bio-friendly OR molecules. By integrating a nonequilibrium photogenerated carrier strategy, high-performance NIR optoelectronic synapses are realized, exhibiting favorable synaptic characteristics, including quasi-linear time-dependent photocurrent generation, extended photocurrent decay, and low energy consumption. Furthermore, the real-time neuromorphic NIR imaging array (12 × 12) based on the FASnI₃-QR perovskite film is successfully developed. By leveraging the enhanced synaptic characteristics and the favorable penetration capability of NIR light, the real-time neuromorphic NIR imaging array realizes neuromorphic imaging, image preprocessing, object recognition, enhance, in-sensor motion perception in complex environments for intelligent autonomous driving and surveillance. This work paves the way for lead-free perovskites in the realm of intelligent imaging and provides a roadmap for heterogeneous integration of perovskite optoelectronic synapse and Si electronic circuits.

Methods

Materials

All materials utilized in this study are employed without further purification, which included Au (99.999%, ZhongNuo Advanced Material (Beijing) Technology Co., Ltd), QR (99.9%, Sigma-Aldrich), DMSO (super dehydrated, Sigma-Aldrich), formamidinium iodide (FAI, 99.9%, Advanced Eletion Technology Co., Ltd), black conductive tips (Cat No. 3020201, Zhejiang Saining Biotechnology Co., Ltd.), acetonitile (99.9%, Canrd Technology Co. Ltd), pyromeconic acid (99.9%, Shanghai Titan Scientific Co., Ltd), catechol (99.9%, Energy Chemical), salicylaldehyde (99.8%, J&K Scientific Ltd), formamidinium Bromide (FABr, 99.9%, Advanced Eletion Technology Co., Ltd), SnF₂ (99%, Sigma-Aldrich), pipette (model: 4640060BL, Bioland), Acetone (99.9%, Cat No. 100013, Macklin, Shanghai, China), P-Aminobenzoic Acid (Cat No. JS0568, HongKong JiSiEnBei International Trade Co.,

Limited), tin powder (99.8%, Sigma-Aldrich), iodine (99.8%, Advanced Eletion Technology Co., Ltd), ITO (Advanced Eletion Technology Co., Ltd), zinc acetate (99.9%, Nanjing Zhiyan Technology Co., Ltd), ethanolamine (99.9%, Sigma-Aldrich), polymethyl Methacrylate (99.9%, Nanjing Zhiyan Technology Co., Ltd), PTAA (Nanjing Zhiyan Technology Co. Ltd), ICBA (99.9%, 1-material), sample vial (Cat No. X100001, Leyan, Shanghai, China), 2,2,2-Trifluoroethanol (TFE, Cat No. 269931, 99.8%, J&K Scientific Ltd), Dimethylsulfoxide-d6 (DMSO-d6, Cat No. C400002, Leyan, Shanghai, China), SEM specimen mounts (Zhong-jingkeyi (Beijing) Film Technology Co.,Ltd).

Synthesis of ZnO solutions

A ZnO precursor solution was prepared via the sol-gel method by dissolving 100 mg of zinc acetate and 27 μ L of ethanolamine in 973 μ L of 2-methoxyethanol, followed by stirring for 5 h.

Synthesis of SnI₂ solutions

 Snl_2 solutions were prepared by reacting iodine (431.4 mg) with tin (220.94 mg) in 2 mL of DMSO, with the mixture being stirred for 5 h in a glovebox.

Preparation of hole-only and electron-only devices

Electron-only devices were fabricated with device configuration of ITO/ZnO/Perovskite /ICBA/Ag. Hole-only devices were fabricated with device configuration of ITO/PEDOT:PSS/Perovskite /PTAA/Ag.

Preparation of perovskite films

A 0.85 M FASnI $_3$ perovskite precursor solution was prepared by dissolving 292.5 mg of FAI and 39.98 mg of SnF $_2$ in 2 mL of SnI $_2$ solution, followed by stirring for 5 h at room temperature. A FASnI $_3$ -QR perovskite precursor was obtained by dissolving different amounts of quercetin in the FASnI $_3$ perovskite precursor solution. The perovskite precursor solution was then deposited onto the substrate via spin-coating at 1000 rpm for 12 s, followed by 5000 rpm for 60 s. At 40 s into the spin-coating process, 135 μ L of chlorobenzene was introduced onto the perovskite film. The film was subsequently annealed at 70 °C for 15 min.

Film characterization

UV-Vis absorption spectra were recorded using an Agilent Cary 60 UV-Vis spectrophotometer. PL and TRPL decay measurements were performed with an Edinburgh FLS980 spectrometer. ¹H NMR spectra were obtained on a JEOL JNM-ECZ500R (500 MHz) spectrometer, with DMSO-d₆ as the solvent. AFM images were acquired using a Bruker Dimension Icon in tapping mode. XRD patterns were recorded using a power X-ray diffractometer (D-POWER, GKINST Co., LTD.). Surface elemental compositions and valence states were analyzed using XPS a Thermo Scientific ESCALAB 250Xi, utilizing nonmonochromated Al Ka X-ray radiation as the excitation source. The hyperspectral imaging data were acquired using the WAYHO Visible and NIR Hyperspectral Camera SHIS-N220 (Shenzhen Zhongdarihe Technology Co., Ltd., Shenzhen, China). FTIR spectra were collected with a Thermo Scientific NICOLET iS50 FT-IR spectrometer. TA measurements were obtained by Vitara T-Legend Elite-TOPAS-Helios-EOS-Omni. The pump light wavelengths were 450 nm, while the probe wavelengths, ranging from 470 nm to 1000 nm, were generated by directing the laser beam onto a CaF₂ plate. KPFM was performed on commercial atomic force microscopy (multi-Mode 8, Bruker) using conductive tip (NSC18, MikroMasch, Au-coated, spring constant: 2.8 N m⁻¹, frequency: 75 kHz). CV measurements were performed using a CHI600 electrochemical workstation. An Ag/AgCl electrode served as the reference electrode, a carbon rod coated with the sample was used as the working electrode, and a platinum wire acted as the auxiliary electrode. A 0.1M solution of tetra-n-butylammonium hexafluorophosphate, deoxygenated, was employed as the electrolyte. The

scan rate was set to 500 mV s⁻¹. Potentials of ferrocenium/ferrocene ($FeCp_2^{0/+}$) were used as an internal standard. The HOMO energy levels were obtained by $E_{\text{HOMO}} = -[E_{\text{ox}} + (4.8 - E_{\text{F}_c})]\text{eV}$, the LOMO energy levels were obtained by $E_{\text{LUMO}} = -[E_{\text{red}} + (4.8 - E_{\text{F}_c})]\text{eV}$, where E_{ox} and E_{red} are the onsets of oxidation and reduction potential, respectively.

Preparation of synaptic devices and array

After UV ozone treatment of the cleaned Si/SiO $_2$ substrates for 30 min, PEDOT:PSS was spin-coated at 4000 rpm for 30 s and annealed at 150 °C for 20 min. The perovskite layer was then deposited in a glove box. 70 nm gold layer was obtained by vacuum deposition at a deposition rate of $0.05~\text{Å}~\text{s}^{-1}$ with device area of $1000~\mu\text{m} \times 200~\mu\text{m}$. The TFT backplane and readout system was provided by LinkZill Technology Co., Ltd (SC-T-A064-2203). The array was obtained through the heterogeneous integration of perovskite optoelectronic synaptic device and Si electronic circuits. To ensure stability, the fabricated arrays were encapsulated to provide insulation against water and oxygen.

Devices measurements

The electrical outputs of the encapsulated devices were systematically recorded using a semiconductor parameter analyzer (Platform Design Automation, PDA FS380 Pro). The square-wave pulsed light with different pulse width and frequency was generated by an arbitrary function generator (INSTEK AFG-2005). The ball trajectory was captured using the SH3-101 High-Speed Camera (SinceVision Technology Co., Ltd., Shenzhen, China), serving as a reference device. Electrochemical characterization was conducted with a PAIOS 4.1 instrument.

DFT calculations

All DFT calculations were performed by using the Vienna Ab initio Simulation Package. The exchange-correlation function was based on the generalized gradient approximation with the Perdew-Burke-Ernzerhof functional. The passivated molecule was positioned above the perovskite surface with a distance of more than 2.5 Å prior to relaxation. In order to avoid interactions between adjacent images, the vacuum laver was set more than 20 Å along z-axis. The cutoff energy for plane-wave basis was set as 400 eV and the energy convergence criterion was set as 10⁻⁶ eV. The supercell bottom atoms were fixed while others were fully relaxed until the force tolerance less than 0.03 eVÅ⁻¹. Taking obvious function of van der Waals into considering, semi-empirical DFT-D3 approach was used to correct in all calculations. Charge transfer between the passivated molecule and the host material was assessed using Bader charge analysis. The structure of quercetin was optimized using the 6-31 G basis set and the B3LYP functional, and the charge distribution was determined with Gaussian 09 W. To illustrate the ESP on the van der Waals surface of the molecule, a color-coded iso-surface plot was generated using the Visual Molecular Dynamics software.

The adsorption energy of quercetin on the surface of the host material was determined as follows:

$$E_{\text{abs}} = E_{\text{perfect + passiivator}} - E_{\text{perfect}} - E_{\text{passivator}}$$
 (5)

Where $E_{\rm perfect+passivator}$, $E_{\rm perfect}$, $E_{\rm passivator}$ denotes the total energy of passivated system by additive, perfect crystal, and passivated molecule, respectively.

To assess the impact of passivation on vacancy defect accessibility, we computed the vacancy formation energies for FASnl₃ slabs both with and without passivation:

$$\Delta E_{\rm f} = E_{\rm vacany} + E_{\rm perfect} + E_{\rm Sn} \tag{6}$$

where E_{vacancy} , E_{perfect} represent the total energy of slab with a vacancy, and the total energy of pristine structure, respectively. E_{Sn} is the energy of single Sn referring to solid phase.

Data availability

All data supporting the findings of this study are available within the article and its Supplementary Information files, or from the corresponding author, X.M. (mengxiangyue@ucas.ac.cn). Additional raw data are not publicly available at this time, as they are currently under consideration for intellectual property protection and potential patent filing. Access to these data is restricted to safeguard the novelty of the technology and to comply with institutional IP policies. Requests for access to the restricted data may be submitted to the corresponding author via email. Access will be granted on a case-by-case basis, subject to approval by the authors' institution, and is limited to noncommercial academic research purposes only. The data can only be shared with researchers affiliated with recognized academic or research institutions and may not be used for commercial purposes. We aim to respond to access requests within 10 business days. Once approved, the data will remain accessible to the requester for a period of 12 months. Extensions may be considered upon request.

References

- Huang, H. et al. Fully integrated multi-mode optoelectronic memristor array for diversified in-sensor computing. *Nat. Nanotechnol.* 20, 93–103 (2025).
- Ren, Q. et al. Optoelectronic devices for in-sensor computing. Adv. Mater. https://doi.org/10.1002/adma.202407476.
- 3. Zhou, F. & Chai, Y. Near-sensor and in-sensor computing. *Nat. Electron.* **3**, 664–671 (2020).
- Cho, S. W., Jo, C., Kim, Y.-H. & Park, S. K. Progress of materials and devices for neuromorphic vision sensors. *Nano-Micro Lett.* 14, 203 (2022).
- Marković, D., Mizrahi, A., Querlioz, D. & Grollier, J. Physics for neuromorphic computing. *Nat. Rev. Phys.* 2, 499–510 (2020).
- Chen, J. et al. Optoelectronic graded neurons for bioinspired in-sensor motion perception. *Nat. Nanotechnol.* 18, 882–888 (2023).
- Lee, J. et al. Thin-film image sensors with a pinned photodiode structure. Nat. Electron. 6, 590–598 (2023).
- 8. Tang, J. et al. Bridging biological and artificial neural networks with emerging neuromorphic devices: fundamentals, progress, and challenges. *Adv. Mater.* **31**, 1902761 (2019).
- Long, Z. et al. Biomimetic optoelectronics with nanomaterials for artificial vision. Nat. Rev. Mater. 10, 128–146 (2025).
- He, K., Wang, C., He, Y., Su, J. & Chen, X. Artificial neuron devices. Chem. Rev. 123, 13796–13865 (2023).
- Ding, G. et al. Nanomaterials for flexible neuromorphics. Chem. Rev. 124, 12738–12843 (2024).
- Xu, M. et al. Reconfigurable neuromorphic computing: materials, devices and integration. Adv. Mater. 35, 2301063 (2023).
- Lee, Y. et al. A low-power stretchable neuromorphic nerve with proprioceptive feedback. Nat. Biomed. Eng. 7, 511–519 (2023).
- Kim, S. J. et al. Linearly programmable two-dimensional halide perovskite memristor arrays for neuromorphic computing. *Nat. Nanotechnol.* 20, 83–92 (2025).
- Choi, C. et al. Curved neuromorphic image sensor array using a MoS₂-organic heterostructure inspired by the human visual recognition system. *Nat. Commun.* 11, 5934 (2020).
- Ouyang, B. et al. Bioinspired in-sensor spectral adaptation for perceiving spectrally distinctive features. *Nat. Electron.* 7, 705–713 (2024).
- 17. Liu, Z. et al. All-in-one optoelectronic transistors for bio-inspired visual system. *Adv. Mater.* **36**, 2409520 (2024).

- Chen, K. et al. Organic optoelectronic synapse based on photonmodulated electrochemical doping. *Nat. Photonics* 17, 629–637 (2023).
- Wang, S. et al. An organic electrochemical transistor for multimodal sensing, memory and processing. *Nat. Electron.* 6, 281–291 (2023).
- 20. Liu, K. et al. An optoelectronic synapse based on α -In₂Se₃ with controllable temporal dynamics for multimode and multiscale reservoir computing. *Nat. Electron.* **5**, 761–773 (2022).
- Zhu, X., Li, D., Liang, X. & Lu, W. D. Ionic modulation and ionic coupling effects in MoS₂ devices for neuromorphic computing. *Nat. Mater.* 18, 141–148 (2019).
- Zhou, H., Li, S., Ang, K.-W. & Zhang, Y.-W. Recent advances in inmemory computing: exploring memristor and memtransistor arrays with 2D materials. *Nano-Micro Lett.* 16, 121 (2024).
- Vasilopoulou, M. et al. Neuromorphic computing based on halide perovskites. Nat. Electron. 6, 949–962 (2023).
- Zhu, H. et al. Tin perovskite transistors and complementary circuits based on A-site cation engineering. Nat. Electron. 6, 650–657 (2023).
- 25. Liu, S. et al. An ultrasmall organic synapse for neuromorphic computing. *Nat. Commun.* **14**, 7655 (2023).
- Xu, W. et al. Organometal halide perovskite artificial synapses. Adv. Mater. 28, 5916–5922 (2016).
- Wang, Y. et al. Photonic synapses based on inorganic perovskite quantum dots for neuromorphic computing. Adv. Mater. 30, 1802883 (2018).
- Zhu, Q.-B. et al. A flexible ultrasensitive optoelectronic sensor array for neuromorphic vision systems. Nat. Commun. 12, 1798 (2021).
- Wang, C. et al. Strain-insensitive viscoelastic perovskite film for intrinsically stretchable neuromorphic vision-adaptive transistors. Nat. Commun. 15, 3123 (2024).
- Guo, L. et al. Two-terminal perovskite optoelectronic synapse for rapid trained neuromorphic computation with high accuracy. Adv. Mater. 36, 2402253 (2024).
- Leng, Y.-B. et al. A near-infrared retinomorphic device with high dimensionality reservoir expression. Adv. Mater. 36, 2411225 (2024).
- Hong, X., Liu, X., Liao, L. & Zou, X. Review on metal halide perovskite-based optoelectronic synapses. *Photonics Res.* 11, 787–807 (2023).
- 33. Cao, F. et al. Dual-functional perovskite-based photodetector and memristor for visual memory. *Adv. Mater.* **35**, 2304550 (2023).
- 34. Shao, H. et al. Reconfigurable optoelectronic synaptic transistor with stable Zr-CsPbI₃ nanocrystals for visuomorphic computing. *Adv. Mater.* **35**, 2208497 (2023).
- 35. Zhang, F. et al. Photoinduced nonvolatile memory transistor based on lead-free perovskite incorporating fused Π-conjugated organic ligands. *Adv. Mater.* **36**, 2307326 (2024).
- Chen, J. et al. Efficient tin-based perovskite solar cells with transisomeric fulleropyrrolidine additives. *Nat. Photonics* 18, 464–470 (2024).
- 37. Yu, D. et al. Electron-withdrawing organic ligand for high-efficiency all-perovskite tandem solar cells. *Nat. Energy* **9**, 298–307 (2024).
- 38. Wu, W. et al. Flexible photodetector arrays based on patterned CH3NH3Pbl3-Cl perovskite film for real-time photosensing and imaging. *Adv. Mater.* **31**, 1805913 (2019).
- Liu, J. et al. A bioinspired flexible neuromuscular system based thermal-annealing-free perovskite with passivation. *Nat. Commun.* 13, 7427 (2022).
- Min, H. et al. Additive treatment yields high-performance lead-free perovskite light-emitting diodes. Nat. Photonics 17, 755–760 (2023).
- 41. Li, Y. & Shen, G. Advances in optoelectronic artificial synapses. *Cell Rep. Phys. Sci.* **3**, 101037 (2022).
- 42. Fei, C. et al. Lead-chelating hole-transport layers for efficient and stable perovskite minimodules. *Science* **380**, 823–829 (2023).

- 43. Srivastava, N., Bansal, A., Aggarwal, K. & Nagpal, K. Development and validation of UV spectrophotometric method for the quantitative estimation of quercetin in bulk followed by its solubility studies. *J. Appl. Spectrosc.* **91**, 700–708 (2024).
- 44. Prutskij, T. et al. Concentration-dependent fluorescence emission of quercetin. *Chemosensors* **9**, 315 (2021).
- 45. Wang, N. et al. Perovskite light-emitting diodes based on solution-processed self-organized multiple quantum wells. *Nat. Photonics* **10**, 699–704 (2016).
- 46. Wang, S. et al. Stabilization of perovskite lattice and suppression of Sn²⁺/Sn⁴⁺ oxidation via formamidine acetate for high efficiency tin perovskite solar cells. Adv. Funct. Mater. 33, 2215041 (2023).
- Cheng, W., He, X., Wang, J.-G., Tian, W. & Li, L. N -(2-aminoethyl) acetamide additive enables phase-pure and stable α-FAPbl₃ for efficient self-powered photodetectors. *Adv. Mater.* 34, 2208325 (2022).
- 48. He, M. et al. Sn-based self-powered ultrafast perovskite photodetectors with highly crystalline order for flexible imaging applications. *Adv. Funct. Mater.* **33**, 2300282 (2023).
- Meng, X. et al. Surface-controlled oriented growth of FASnI₃ crystals for efficient lead-free perovskite solar cells. *Joule* 4, 902–912 (2020).
- 50. Kim, Y. et al. A bioinspired flexible organic artificial afferent nerve. *Science* **360**, 998–1003 (2018).
- Liu, C.-K. et al. Lead-free perovskite/organic semiconductor vertical heterojunction for highly sensitive photodetectors. ACS Appl. Mater. Interfaces 12, 18769–18776 (2020).
- 52. Xie, C., You, P., Liu, Z., Li, L. & Yan, F. Ultrasensitive broadband phototransistors based on perovskite/organic-semiconductor vertical heterojunctions. *Light Sci. Appl.* **6**, e17023 (2017).
- 53. Wang, S. et al. Retina-inspired organic photonic synapses for selective detection of SWIR light. *Angew. Chem. Int. Ed.* **62**, e202213733 (2023).
- 54. Chen, H., Cai, Y., Han, Y. & Huang, H. Towards artificial visual sensory system: organic optoelectronic synaptic materials and devices. *Angew. Chem. Int. Ed.* **63**, e202313634 (2024).
- 55. Liu, T. et al. Multifunctional organic vertical photodiodes for photodetection and photo-synapse enabled by modulation of the interface energy barrier. *Adv. Opt. Mater.* **10**, 2201104 (2022).
- Fuller, E. J. et al. Parallel programming of an ionic floating-gate memory array for scalable neuromorphic computing. Science 364, 570–574 (2019).
- 57. Wu, X. et al. Ultralow-power optoelectronic synaptic transistors based on polyzwitterion dielectrics for in-sensor reservoir computing. *Sci. Adv.* **10**, eadn4524 (2024).
- Gao, Z. et al. Tunable negative and positive photoconductance in Van Der Waals heterostructure for image preprocessing. Adv. Mater. 36, 2401585 (2024).
- Wang, Y. et al. Monolithic 2D perovskites enabled artificial photonic synapses for neuromorphic vision sensors. Adv. Mater. 36, 2311524 (2024).
- 60. Wei, B. et al. Ultra-low power MoS₂ optoelectronic synapse with wavelength sensitivity for color target recognition. Sci. China Inf. Sci. **68**, 140406 (2025).
- 61. Hou, Y.-X. et al. Large-scale and flexible optical synapses for neuromorphic computing and integrated visible information sensing memory processing. ACS Nano 15, 1497–1508 (2021).
- 62. Guo, Z. et al. Organic high-temperature synaptic phototransistors for energy-efficient neuromorphic computing. *Adv. Mater.* **36**, 2310155 (2024).
- 63. Shi, Q. et al. Printable, ultralow-power ternary synaptic transistors for multifunctional information processing system. *Nano Energy* **87**, 106197 (2021).

- 64. Zhu, X. et al. High-contrast bidirectional optoelectronic synapses based on 2D molecular crystal heterojunctions for motion detection. *Adv. Mater.* **35**, 2301468 (2023).
- Dang, Z. et al. Object motion detection enabled by reconfigurable neuromorphic vision sensor under ferroelectric modulation. ACS Nano 18, 27727–27737 (2024).
- Deng, M., Li, Z., Liu, S., Fang, X. & Wu, L. Wafer-scale integration of two-dimensional perovskite oxides towards motion recognition. *Nat. Commun.* 15, 8789 (2024).
- Zhang, Z. et al. All-in-one two-dimensional retinomorphic hardware device for motion detection and recognition. *Nat. Nanotechnol.* 17, 27–32 (2022).
- 68. Baek, E. et al. Neuromorphic dendritic network computation with silent synapses for visual motion perception. *Nat. Electron.* **7**, 454–465 (2024).

Acknowledgements

T.L. and Z.Y. contributed equally to this work. This work was supported by the National Key R&D Program of China (2024YFB3614300, X.M.), the National Natural Science Foundation of China (22179131, X.M.), the Fundamental Research Funds for the Central Universities, and the University of Chinese Academy of Sciences. A portion of this work is based on the data obtained at BSRF-1W1A. The authors gratefully acknowledge the cooperation of the beamline scientists at BSRF-1W1A beamline.

Author contributions

T.L. and Z.Y. contributed equally to this work. Y.C. and X.M. proposed and supervised the project. X.M. provided funding support. T.L. designed experiments and conceived the idea. T.L. and Z.Y. performed the experiments and data analysis. L.W. synthesized the precursor solution and collected data. C.S., H.C. and H.W. trained the neural networks. Q.Z. and L.H. conducted DFT calculations. W.W. assisted with the data processing. T.L., C.Y. and X.M. wrote the manuscript and all authors provided comments and contributions.

Competing interests

The authors declare no competing interests.

Additional information

Supplementary information The online version contains supplementary material available at https://doi.org/10.1038/s41467-025-59624-2.

Correspondence and requests for materials should be addressed to Yang Chai or Xiangyue Meng.

Peer review information *Nature Communications* thanks Ho Won Jang and Hao-Wu Lin for their contribution to the peer review of this work. A peer review file is available.

Reprints and permissions information is available at http://www.nature.com/reprints

Publisher's note Springer Nature remains neutral with regard to jurisdictional claims in published maps and institutional affiliations.

Open Access This article is licensed under a Creative Commons Attribution-NonCommercial-NoDerivatives 4.0 International License, which permits any non-commercial use, sharing, distribution and reproduction in any medium or format, as long as you give appropriate credit to the original author(s) and the source, provide a link to the Creative Commons licence, and indicate if you modified the licensed material. You do not have permission under this licence to share adapted material derived from this article or parts of it. The images or other third party material in this article are included in the article's Creative Commons licence, unless indicated otherwise in a credit line to the material. If material is not included in the article's Creative Commons licence and your intended use is not permitted by statutory regulation or exceeds the permitted use, you will need to obtain permission directly from the copyright holder. To view a copy of this licence, visit https://creativecommons.org/licenses/by-nc-nd/4.0/.

© The Author(s) 2025